Eurographics / ACM SIGGRAPH Symposium on Computer Animation (2016)
Ladislav Kavan and Chris Wojtan (Editors)

Accurate Simulation of Wound Healing and Skin Deformation

Stefan Feess †, Kathrin Kurfiss, and Dominik L. Michels ‡

Department of Computer Science, Stanford University

Abstract

We devise a method for the accurate simulation of wound healing and skin deformation. This is based on adequate formulations modeling the underlying biological processes. Cell movements and proliferation are described by a biochemical model whereas a biomechanical model covers effects like wound contraction and the influence of the healing process on the surrounding skin. The resulting simulation framework is very efficient and can be used with realistic input parameters like those measured in biochemistry and biophysics. The accurate behavior of our approach is shown by reproducing regenerative healing processes as well as specific effects such as anisotropic wound contraction, scarring and scab formation. Its efficiency and robustness is illustrated on a broad spectrum of complex examples.

Categories and Subject Descriptors (according to ACM CCS): I.3.7 [Computer Graphics]: Three-Dimensional Graphics and Realism—Animation I.3.5 [Numerical Methods]: Computational Geometry and Object Modeling—Physically based modeling

Keywords: Biochemical models, cell movement, medical simulation, physically based modeling, skin simulation, wound contraction, wound healing.

1. Introduction

While minor skin imperfections like those which are caused by small blackheads, pimples, scars, or warts can be easily taken into account due to the use of appropriate textures and bump maps, realistic complex skin damages and wounds are much harder to include when modeling virtual animals or humans in scientific and visual computing. If their long-term temporal evolution is also of interest, for example for medical purposes or in the case of long story times in films, the dynamic healing process has to be modeled realistically, which requires a sophisticated simulation approach capturing the relevant biochemical and biomechanical processes accurately.

In fact, the healing of wounds is a complex process in which a variety of cells interact to recover the traumatic damage. After the skin tissue gets damaged the body orchestrates a sequence of events to prevent blood loss, clean the wound, and finally grow new tissue into the wound area. The outcome of a healing process, the final shape of the wound and the amount of scarring is dependent on a lot of factors, like the oxygen supply, the initial depth, the wound environment, and the medical treatment when indicated. Although some of the processes are not fully understood yet they have been studied in depth in the fields of biology and physiology. However there has been no attempt made yet to appropriately model a complex healing wound based on those biological insights. In this work we aim to simulate and visualize the different stages a wound undergoes and the effects that certain conditions in those stages will have on the healing process. In particular, our specific contributions are as follows.

1. We introduce an appropriate model describing the biochemical and biomechanical processes of wound healing into the realm of visual computing and solve it numerically in order to simulate such kind of dynamic processes realistically. Thereby, we take the effects of the four different biological phases of wound healing into account, in particular haemostasis, inflammation, proliferation, and maturation.
2. On that basis, we develop an accurate and efficient simulation and visualization framework which can robustly simulate wound healing processes on arbitrary input geometries.
3. We demonstrate the accurate behavior of the presented approach by reproducing regenerative healing processes as well as scarring, keloid overgrowth, scab formation, and anisotropic contraction. Furthermore, to verify its robustness, we apply our method to simulate several complex wound healing scenarios.

2. Related work

Within the visual computing community, a broad range of skin related topics have been covered. From mechanical deformation on macro- (cf. [MZS*11]) and micro-scales (cf. [Nag15]), over muscles (cf. [TBHF03]) and bones including skin sliding effects (cf. [LSNP13]), efficient contact handling and bulging effects from

† E-mail: feess@stanford.edu
‡ E-mail: michels@cs.stanford.edu

muscle contraction (cf. [VBG*13]) over the coupling of a musculoskeletal system with volumetric soft tissue (cf. [LST09]) to clotting and bleeding (cf. [UF11]), and even structural wound syntheses (cf. [LLC11]) and virtual surgery scenarios (cf. [Sif07]). However, to the best of our knowledge the accurate simulation of wound healing has not been addressed in visual computing so far.

In contrast, if one considers appropriate literature in biomedical research, a large amount of publications can be found, that cover single aspects of a wound healing process in depth. Here we want to just highlight a few of them. The first computational model for wound healing was developed in [SM91] where the authors suggest the use of a simple biochemical signaling from a single chemical to regulate the healing process. Then in [OSM95] different interdependent species that affect wound closure and contraction were modeled first. This was later extended in [JMDGA09] with further cell signaling and dynamic mechanical properties based on collagen deposition. For macroscopic deformation, [GOH06] examined the mechanical properties of arterial layers and proposed a hyperelastic model that is also applicable to skin. Next to that [CMU10] proposed a model to simulate scar tissue and account for the fiber direction of the collagen.

3. The Wound Healing Process

In order to enable the reader to better understand the process of wound healing in preparation for studying the biochemical and biomechanical model in this contribution, we briefly describe the relevant phases of haemostasis, inflammation, proliferation, and maturation in this section. Further information can be found in biological and medical literature; for example, an excellent overview is given in [OB09].

The haemostasis process is the first response of the body to a tissue damage aiming to reduce the blood loss and initiating the regeneration. The wounded area fills with blood plasma, platelets and fibrinogen stream in and form a provisional matrix that enables cell migration. At the same time platelets get trapped in the matrix and stick to the open vessels. Also clotting factors, transforming growth factors (TGF-beta) and vascular endothelial growth factors (VEGF), are being released as the platelets come into contact with the damaged tissue. On the surface, the clot starts to dry out and form a scab.

In the following inflammation phase, the wound gets cleaned from foreign particles and bacteria. Monocytes and neutrophils enter the wound. They process bacteria as well as clot in order to enable the growth of new tissue. Monocytes transform into macrophages, consume dead tissue and release macrophage derived growth factors (MDGF).

The new tissue is being created in the following proliferation phase. For that, fibroblasts enter the wound attracted by the growth factors and start to produce collagen, the main component of human skin. Collagen is also the main element for the new extracellular matrix (ECM), which provides the scaffold that allows the vascular network to grow into. This newly formed, soft and fragile mass is typically denoted as granulation tissue. Activated by the growth factors, keratinocytes migrate and start to proliferate. In this so called re-epithelialization, those epithelial cells grow on to the healthy granulation tissue in order to seal the wound with a protective layer. Within the granulation, tissue fibroblasts get transformed by growth factors into myofibroblasts. Those smooth muscle-like cells exert a contractile force on their surrounding. This contraction can reduce the area of a wound by 40 to 80 percent, and so helps to minimize the surface of the exposed flesh.

In a usual healing process the amount of collagen production equalizes with the degradation at some point. In some cases however the apoptotic effect is not strong enough to regulate the amount of collagen. This leads to an excessive collagen deposition, resulting in large tumors or keloid scars, which grow beyond the wound boundaries.

As soon as the wound is closed, the maturation phase begins. In this remodeling step, collagen fibers of type-III, that have been produced quickly by the fibroblasts, gradually get replaced by a much stronger type-I collagen. Also the fibers get rearranged to reach maximal tensile strength. With progressing maturation the scar looses its red color and reaches its final shape and tone.

4. Biochemical and Biomechanical Processes

Our final wound regeneration model can be separated into two parts describing the biochemical and biomechanical processes.

The first one handles the cell movement and the proliferation. Here we reproduce angiogenesis (i.e. the growth of new capillaries), the formation of fibroblasts, wound closure trough an epithelial layer, scab formation, and the generation of fibrous scar tissue. As additional materials, MDGF and oxygen are needed, as they play an important role in the formation of new tissues and heavily influence the other species. Those processes are approximated by diffusion equations with different rates of growth, decay, and dependency on other specimen.

In contrast, the mechanical simulation aims to reproduce the effect of wound contraction that affects the surrounding healthy skin. During the proliferation phase, fibroblasts produce myofibroblasts which start to contract and exert stress on the tissue.

Therefore we need to couple the biochemical simulation with a mechanical one. For that, we deploy the hyperelastic material formulation proposed in [GOH06] for the simulation of arterial layers. For the biochemical processes we adapt the diffusion models of oxygen, MDGF, capillary and fibroblast density as described in [VJGAGB14]. These formulations are extended to model eschar density, epithelial layer, scar tissue density, and dynamic wound regions. The interplay of the simulated species is illustrated in Fig. 1.

4.1. Biochemical Model

In the biochemical part, the angiogenesis process is described by a series of interconnected diffusion equations. We simulate the concentrations of oxygen u_1, MDGF u_2, capillary density u_3, fibroblasts n, eschar density s, scar tissue ρ, epithelium e, and a plasma field p which defines the wound region described by its indicator function ω. A convection process links these quantities to the mechanical simulation and the resulting displacement vector $\mathbf{v}$.

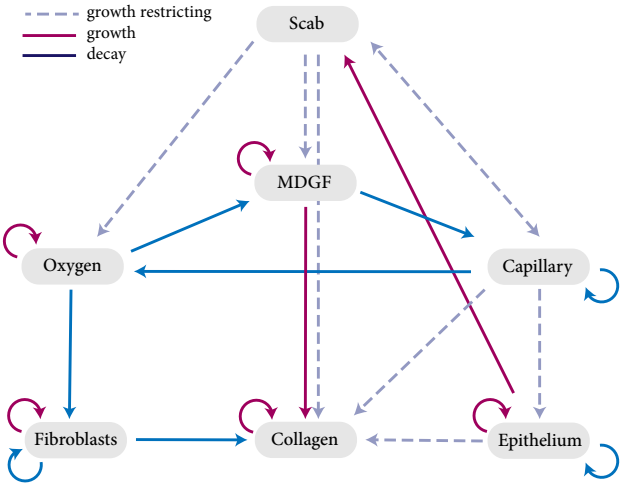

Figure 1: Illustration of the dependencies between the simulated species and how they affect each other regarding growth or death.

4.1.1. Oxygen (u_1)

Oxygen is an important variable in the wound healing process and has a major effect on the angiogenesis; see [KHS*83]. In [VJGAGB14], the influence of oxygen is modeled as a diffusion process which depends on capillary density and decay. We additionally add the inverse dependency on the eschar density since it is a form of necrotic tissue that, if reaching deep into the wound, can hinder the regeneration process until it is dissolved. The process is described by

$$\partial_t u_1 + \nabla \cdot (u_1 \partial_t \mathbf{v}) = (1-s)\left(D_1 \nabla^2 u_1 + \lambda_{3,1} u_3\right) - \lambda_{1,1} u_1$$

with scalar model parameters D_1, $\lambda_{1,1}$, and $\lambda_{3,1}$. Similarly to [JMDGA09, VJGAGB12], the model parameter D_i denotes the diffusion rate of the quantity described by u_i for $i \in \{1,2,3\}$ (e.g. D_1 describes the oxygen diffusion rate). Analogously, $\lambda_{i,j}$ describes the influence of the quantity described by u_i on the quantity described by u_j.

4.1.2. MDGF (u_2)

Macrophages are one of the first cell types which enter the wound. The under-oxygenated tissue attracts them into the wound site and they release growth factors to start the regeneration process. We also add the inverse dependency on the scab here. The process is described by

$$\partial_t u_2 + \nabla \cdot (u_2 \partial_t \mathbf{v}) = (1-s)\left(D_2 \nabla^2 u_2 + \lambda_{1,2} P(u_1)\right) - \lambda_{2,2} u_2$$

with $P(u_1) = 1 - (u_1 / u_1^{\beta_2})$ if $u_1 < u_1^{\beta_2}$ and $P(u_1) = 0$ otherwise. In this context, $u_1^{\beta_2}$ denotes the oxygen concentration below MDGF are produced. This accounts for increased attraction in regions with low oxygen and inhibited MDGF production where oxygen levels returned to normal.

4.1.3. Capillary Density (u_3)

The growth of new capillaries, angiogenesis, is mainly influenced by the MDGF and is reduced with increasing scab density. The process is described by

$$\partial_t u_3 + \nabla \cdot (u_3 \partial_t \mathbf{v}) = (1-s)\left(\left(D_3 \nabla^2 u_3 + \left(\lambda_{3,3} + \lambda_{3,2} u_2\right) u_3 \left(1 - \frac{u_3}{u_3^{eq}}\right)\right)\right),$$

where u_3^{eq} is the maximal capillary density.

4.1.4. Fibroblasts (n)

Fibroblasts are a cell species that is responsible for the synthesis of a new ECM. They produce collagen which makes up (scar-)tissue and differentiate into myofibroblasts, that align and generate contractile forces on the surrounding as described in [GRM71]. Their behavior is described by

$$\partial_t n + \nabla \cdot (n \partial_t \mathbf{v}) = (1-s)\left(D_n \nabla^2 n + r_n u_1 n \left(1 - \frac{n}{K}\right)\right) - \lambda_{n,n} n,$$

in which r_n denotes the maximal rate of fibroblasts proliferation and K the fibroblasts' maximal capacity.

4.1.5. Eschar Density (s)

When the wound does not get covered with a wound dressing to keep it moist, the blood plasma dries out and an eschar forms on the wound surface to provide a temporary coverage. If the scab gets thicker, it takes more time to dissolve the hard eschar first so that the wound healing process is delayed and more fibrotic tissues can form; see [GRC*10]. We model the eschar density as a diffusion that has its source on the exposed wound surface. With progressing granulation and re-epithelialization, the epithelial tongue grows into the wound site and under the scab. Keratinocytes, which later form the new epidermis, start to dissolve the eschar from underneath; see [KWP*01]. This effect is captured in our model by reducing the scab formation with increasing epithelial density. The process is described by

$$\partial_t s + \nabla \cdot (s \partial_t \mathbf{v}) = D_s \nabla^2 s + (1-s)(1-u_3) R(\omega) - \lambda_{e,s} e\, s,$$

in which $R(\omega)$ denotes the interface of the wound region ω.

4.1.6. Epithelium (e)

The epidermis forms the outer layer of the skin and contains no blood vessels. In the healing process it grows on healthy but fragile granulation tissues and forms a protective layer over it. To restrict the growth to healthy granulation tissues we define a function

$$Q_i(u_3) = \begin{cases} \frac{1}{\gamma_1} u_3 & u_3 < \gamma_1, \\ -\frac{1}{1-\gamma_1} u_3 + \frac{1}{1-\gamma_1} & \text{otherwise}, \end{cases}$$

that limits the growth of epithelial cells to a certain region of the capillary density according to a model parameter γ_1. The process is then described by

$$\partial_t e + \nabla \cdot (e \partial_t \mathbf{v}) = Q_i(u_3)\left(D_e \nabla^2 e + \lambda_{g,e} e\right) - \lambda_{e,e} e.$$

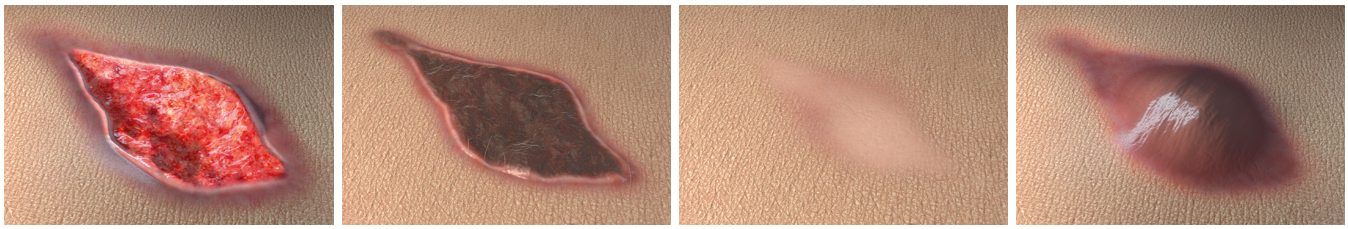

(a) Initial wound shape. (b) Scab formation. (c) Regenerated shape. (d) Keloid scar.

Figure 2: Comparisons of different healing processes. Starting from the identical wound shape (Fig. 2a), we simulated with scab formation (Fig. 2b), a clean regeneration (Fig. 2c), and a collagen overgrowth resulting in a keloid scar (Fig. 2d).

4.1.7. Scar Tissue (ρ)

The provisional collagen type-III produced by fibroblasts gradually gets replaced by tougher type-I collagen which makes up the fibrotic scar; see [CMU10]. Healthy skin also consists of collagen type I, however the fibers in scar tissue are almost uniformly aligned. Not until the remodeling phase begins, the originally random alignment recovers to some degree and the scar gets less visible. Our model relates scar tissue density to fibroblast based collagen production and reduction based on the remodeling over time:

$$\partial_t \rho + \nabla \cdot (\rho\, \partial_t \mathbf{v}) = (1-s)(1-u_3)(1-e)\lambda_{n,\rho} n - \lambda_{\rho,\rho}\rho\,.$$

4.1.8. Wound Region (ω)

To restrict the growth of the cells to a certain area and allow for the overgrowth of keloid scars we model a dynamic wound region ω based on blood plasma. In particular, the wound area is filled by clotted blood. For that we make use of a diffusion model that emits from the wound boundaries. To account for the overgrowth of fibrous tissue, we include a term that adds excessive collagen deposition. Hence, if a certain collagen density is exceeded, this excess is being pushed into the wound region to expand the volume. In the case of a perfect regeneration, we assume that the wound region extends over the entire wounded tissue. For that, in this area we set $\omega = 1$. In the dynamic case, a plasma field p is defined that describes the blood clot which fills the damaged area. The process is expressed by

$$\partial_t p + \nabla \cdot (p\, \partial_t \mathbf{v}) = D_p \nabla^2 p + (\lambda_{p,p} p + C(\rho)(1-p))\,,$$

in which the function $\rho \mapsto C(\rho) := \max(0, \rho - \rho_{\max})/\rho_{\max}$ accounts for an excessive collagen deposition that leads to growing wound boundaries. That way, keloid scar formation can be simulated. Then, we define the wound domain via $\omega = 1$ if $p > p_{min}$ and $\omega = 0$ otherwise.

4.2. Mechanical Contraction Model

During the proliferation phase, the wound contraction sets in to decrease the wound surface. Especially in scars the result of this effect can get clearly visible. The cause for the contraction are cell induced forces that affect the surrounding tissue. It has been shown that myofibroblasts, modified fibroblasts with smooth-muscle like features are mainly involved in this process; see [GRM71]. Here we follow [VJGAGB14] where the myofibroblast exerted stress can be directly deduced form the fibroblasts density. According to that the resulting Cauchy stress tensor is represented by

$$\sigma_{\text{cell}} = \sigma_{\text{cell}} \mathbf{I} = p_{\text{cell}}(\theta) n K_m \mathbf{I}\,,$$

in which $\mathbf{I}$ denotes the second order identity tensor, θ the volumetric strain on the tissue, and K_m an enhancement factor. The active pressure on the tissue as a result of sliding actin and myosin fibers is expressed by $p_{\text{cell}}(\theta)$. The pressure gets maximal when they perfectly align and it proportionally decreases when this overlap is reduced; see [MGAD08]. This is modeled with the piecewise linear constitutive law

$$p_{\text{cell}}(\theta) = \begin{cases} K_{\text{pas}}\theta & \theta < \theta_1\,, \\ \frac{K_{\text{act}} p_{\max}}{K_{\text{act}}\theta_1 - p_{\max}}(\theta_1 - \theta) + K_{\text{pas}}\theta & \theta \le \theta_1 \le \theta^*\,, \\ \frac{K_{\text{act}} p_{\max}}{K_{\text{act}}\theta_2 - p_{\max}}(\theta_2 - \theta) + K_{\text{pas}}\theta & \theta^* < \theta \le \theta_2\,, \\ K_{\text{pas}}\theta & \theta > \theta_2\,, \end{cases}$$

where $\theta^* = p_{\max}/K_{\text{act}}$. Here, θ_1 and θ_2 represent the shortening and lengthening strain, the lower and the upper limit of the contractile element, and the active and passive volumetric stiffness moduli are K_{act} and K_{pas} .

4.3. Hyperelastic Skin Model

An explanation for the macroscopic mechanical properties of skin can be found in its internal microscopic structure. According to [HO10] the elastic properties like nonlinearity and anisotropy relate to two different collagenous fibers. In particular the direction and dispersion of those two fiber families significantly effect the mechanical response of the tissue. Based on this assumptions, in [GOH06] the skin is modeled as a hyperelastic material. They propose the strain energy function

$$\overline{\Psi}(\overline{\mathbf{C}}, H_i) = \overline{\Psi}_g(\overline{\mathbf{C}}) + \sum_{i=1}^{2} \overline{\Psi}_{fi}(\overline{\mathbf{C}}, \mathbf{H}_i(\mathbf{a}_{0i}, \kappa))\,,$$

where Ψ_g denotes the isotropic energy and Ψ_{fi} the anisotropic contribution of the fiber family, $i \in \{1,2\}$. Those energy functions proposed by [GOH06] depend on the Cauchy-Green tensor $\overline{\mathbf{C}}$, the fiber distribution $\mathbf{H}_i$, the fiber orientation $\mathbf{a}_{0i}$, and on κ, a measure for anisotropy. For damaged skin, [VJGAGB12] adapts the energy function to a linear dependency on the tissue density, so that the resulting strain energy for healing skin is described by $\psi = \hat{\psi}\rho_{ecm}/\hat{\rho}_{ecm}$, where ρ_{ecm} describes the density of the damaged and $\hat{\rho}_{ecm}$ the density of the undamaged skin.

Figure 3: Scarring on a woman's neck resulting from large wounds. This kind of traumata could, for example, be caused by an animal attack.

5. Implementation

In this section, we address the relevant implementation details.

5.1. Biochemical Simulation

The chemical simulation is solved on a regularly spaced three-dimensional Eulerian grid to be able to solve the diffusion processes easily using central differences. We initialize the grid with a user defined input mesh that provides skin and wound object. Then we check with a ray intersection test which cells are wound, skin, or empty cells. After that we add a layer of two cells on top of the skin cells to initialize the epithelial field. This information is stored in a state field that indicates the cell type (empty, epidermis, dermis, or inner/outer bounds) to be able to check for boundaries. An update step then performs the convection of the species along the mechanical displacement, the diffusion processes, and the calculation of the volumetric strain.

5.2. Mechanical Simulation

The mechanical simulation is implemented as a mass-spring system. To simulate the skin as a volumetric object, the input mesh is tetrahedralized first. For this we employ the tetrahedral mesh generator *TetGen* (cf. [Si15]) using a maximal volume constraint to ensure evenly sized tetrahedrons throughout the mesh. In the next step we sample the volumetric strain calculated on the grid onto all endpoints of the springs. This is done with the weight function $\theta_p = \sum_i \phi_i(x_p)\theta_i$. We calculate the volumetric strain energy for every spring and use it to set the new rest-lengths. To get the anisotropic contraction effect, we weight the energy of all fiber directions onto the springs according to their direction. We calculate the resulting energy per spring with a simple angle dependent weighting

$$\Psi_e = \Psi_g + \left\| \frac{\mathbf{a}_{01} \cdot \frac{\mathbf{e}}{\|\mathbf{e}\|}}{\|\mathbf{e}\|} \right\| \Psi_{f1} + \left\| \frac{\mathbf{a}_{02} \cdot \frac{\mathbf{e}}{\|\mathbf{e}\|}}{\|\mathbf{e}\|} \right\| \Psi_{f1} \,,$$

in which $\mathbf{e}$ denotes the spring vector. Now the new rest lengths are set according to $\Delta l = \sqrt{2\Psi_e/k}$, where k denotes the spring stiffness. This follows from enforcing energy conservation. In an update step we perform sub-steps independent from the biochemical part until a stable configuration is reached.

5.3. Grid-Point Coupling

We solve for the convection term in the biochemical diffusion models and transfer the cell strain to the mechanical simulation. For that, we need to couple the deforming mass-spring system with the biochemical simulation. Hence a weighting kernel is needed that transfers particle values onto the grid. For this interpolation we deploy a cubic B-Spline basis function

$$\phi(x) = \begin{cases} \frac{1}{2}(wx)^3 - (wx)^2 + \frac{2}{3}, & 0 < |x| < 1 \,, \\ -\frac{1}{6}(wx)^3 + (wx)^2 - 2wx + \frac{4}{3}, & 1 < |x| < 2 \,, \\ 0, & \text{otherwise} \end{cases}$$

as suggested in [SKB08]. We extend this with a variable kernel size, which depends on the ratio of the grid and the mechanical resolution. Here, we make use of the parameter $w = \sqrt[3]{N_c/N_m}$ with N_m, the total number of spring nodes and N_c, the total number of active grid cells. This one-dimensional construction can be expanded to the multi-dimensional case by their tensor products, so that the final weight function is given by

$$\phi_i(x_p) = \phi(\frac{1}{h_x}(x_p - ih))\phi(\frac{1}{h_y}(y_p - jh))\phi(\frac{1}{h_z}(z_p - kh)) \,,$$

where h is the cell size, $(x_p, y_p, z_p)^\mathsf{T}$ the particle position in grid coordinates, and (i, j, k) the grid index triple.

5.4. Visualization

To visualize the results, we map the simulated fields back onto the original, undeformed mesh in order to apply a displacement and compute the shader accordingly. To define the displacement depth we calculate the normal distance of the surface to the maximal height of a healthy capillary tissue. By adjusting the minimal capillary density threshold it is also possible to artistically influence the displaced wound depth. By sampling the grid we then transfer the other attributes onto the input mesh. With the epithelial cell density we define the shading of wound edges and the healthy skin which overlays the granulation tissue shader. With beginning fibrosis, the scar shader gets blended over dependent on the scar tissue density. For keloids this shader is also dependent on the wound depth to brighten regions that rise further from the surface. At last, the deformation of the mechanical simulation is being transferred to the

original mesh. To allow for more control over the final look, all parameters that go into the shader can be ramped and multiplied. This way we give the user artistic control to delay, speed up, smooth or crease certain regions.

6. Numerical Examples

In this section we present a variety of wound healing scenarios in order to illustrate the capabilities of our approach. We make use of biochemical and biomechanical parameters as those listed in [VJ-GAGB12].

As a first canonical example we show a healing process that is close to a perfect regeneration. Especially for young children, wounds can heal with little to no scarring. We assume here, that the wound is covered with a wound dressing so that no scab will form. In this moist healing environment and without any further contamination the conditions are optimal to minimize the amount of scar formation. Moreover, we assume that there is no tendency for keloid scarring and set a static wound region according to that. As expected, the result is a clean regenerated shape with just little fibrotic tissue that fades over time; see Fig. 2c. We can also observe that the upper region with just shallow wounding exhibits almost no fibrotic tissue. The computation times are listed in Tab. 1 and the temporal evolution of the normalized wound area and its relative error for different temporal step sizes are illustrated in Fig. 4.

A second example shows the overgrowth of the fibrotic tissue. Here we can see that the critical threshold of collagen density is exceeded and therefore the wound region expands, making space for the proliferating collagen. Like in the first example we can see the relation of the wound depth to the amount of scar formation; see Fig. 2d. Excessive collagen production is primarily located in deeply wounded areas leading to a keloid scar.

In a third example we focus on the contraction. We can see that it effects the surrounding healthy tissue and pulls the wound edges together. Also the anisotropic behavior can clearly be observed here. The fibers are set to be aligned horizontally, which leads to stronger contraction in the horizontal direction and an elongated instead of a round wound shape; see Fig. 7.

		Intialization		**Simulation**	
Resolution	**#Tet**	bio.	mech.	bio.	mech.
$(20,15,19)$	4511	0.009	0.287	0.004	0.003
$(40,31,39)$	6350	0.485	0.415	0.018	0.010
$(80,62,79)$	11725	3.626	0.889	0.128	0.079
$(160,124,159)$	34185	29.541	5.243	0.684	0.638
$(320,248,319)$	103111	233.217	41.860	5.356	5.328

Table 1: Overview of the computation times for simulating the clean regeneration process illustrated in Fig. 2 with different grid resolutions/different numbers of tetrahedra approximating the 2cm $\times$ 2cm wound area. The computation times for the initialization process/simulation times per frame for the biochemical and the biomechanical model are listed separately. The computations times are measured in seconds on an Intel(R) Xeon E5 3.5 GHz with 32 GB DDR-RAM without GPU parallelization.

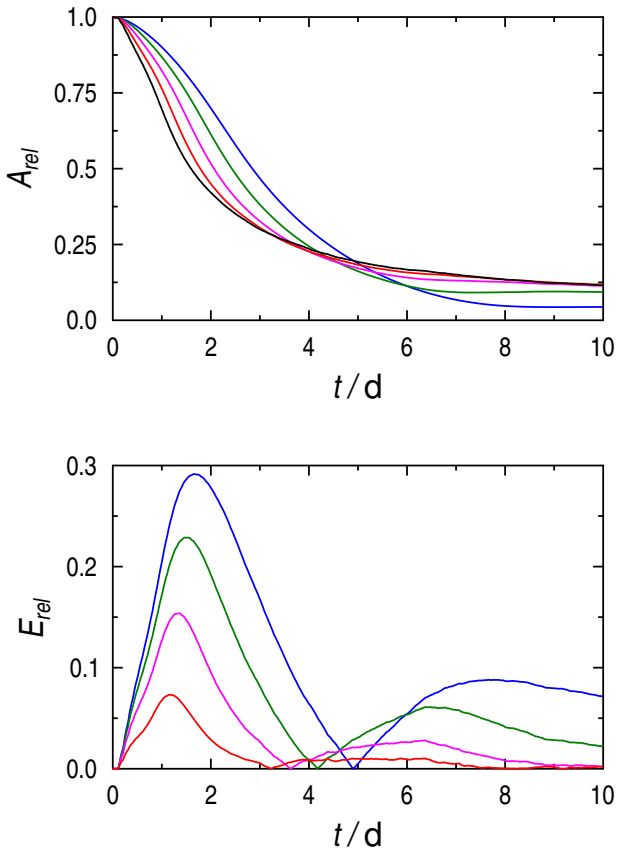

Figure 4: Temporal evolution of the normalized wound area during the first ten days of the clean regeneration process illustrated in Fig. 2 using different temporal step sizes (upper diagramm): $9.375 \cdot 10^{-4}$ days (black curve), $1.875 \cdot 10^{-3}$ days (red curve), $3.75 \cdot 10^{-3}$ days (pink curve), $7.5 \cdot 10^{-3}$ days (green curve), and $1.5 \cdot 10^{-2}$ days (blue curve). The corresponding temporal evolution of the relative error is illustrated in the lower diagram. The measurement with a temporal step size of $9.375 \cdot 10^{-4}$ days is used as the ground truth, since a reduction of the step size below this threshold does not lead to a significant change of the temporal evolution of the wound area.

A fourth example shows the result of a simulation with a complex input geometry. Here we input the mesh of an already scarred face into our simulation framework in order to demonstrate its interaction with the growth processes and its effects on non-smooth geometry; see Fig. 5. We intensionally disable the scab formation here to make the underlying process visible. We can see how the bright red granulation tissue forms and fills the wound. At the same time re-epithelialization can be observed and epithelial cells start to cover the newly formed tissue. This is visualized as the light red edge surrounding the granulation tissue. Next to that the contraction sets in and we can see that there is a maximal stress where the wound is deepest. This is plausible as more fibroblast are being produced in those areas leading to greater volumetric stress. Also some anisotropy in the contraction is visible leading to an elongated scar instead of a contraction to a center point. Towards the end when

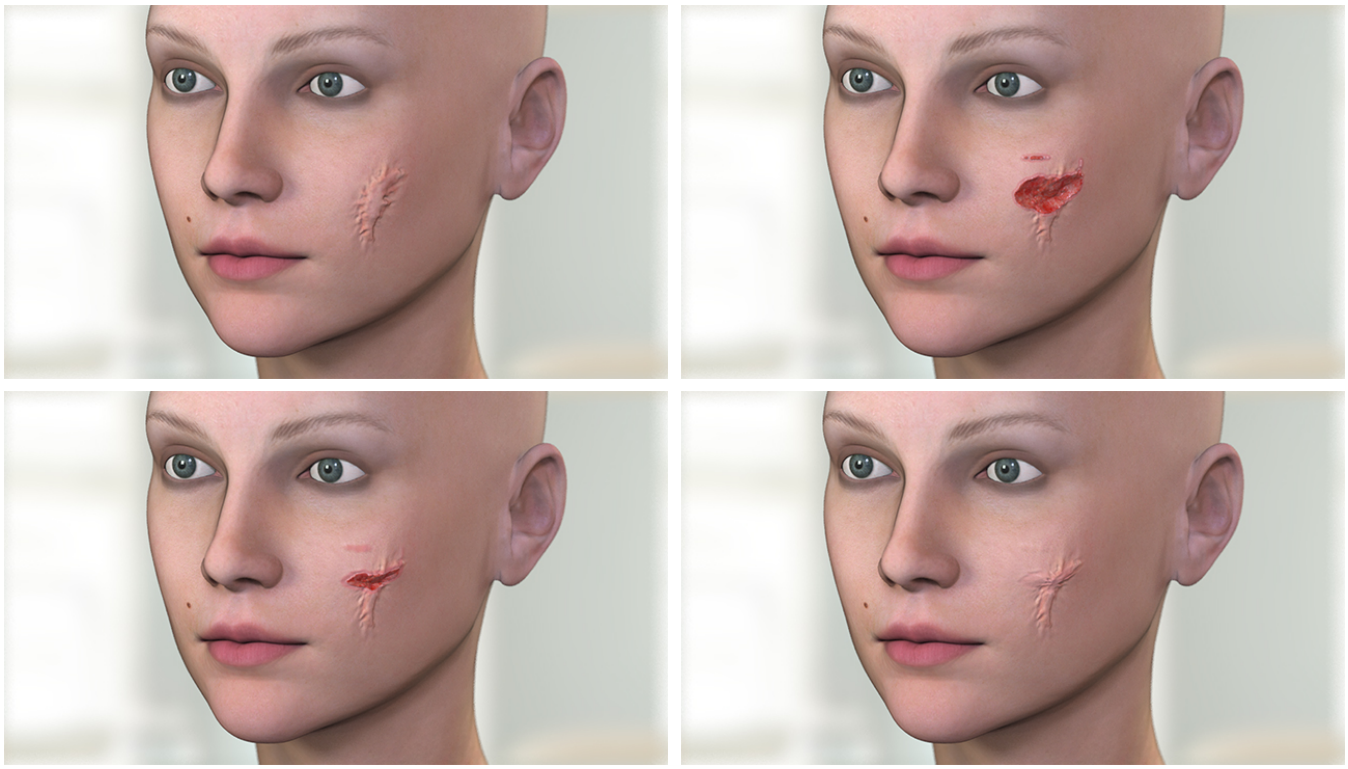

Figure 5: Wound healing on a scarred face in order to show the different effects on a complex geometry. The input geometry (upper left picture) is violated (upper right picture) and their healing process is simulated and visualized (lower pictures). To make the whole process visible we disabled the scab formation. As the healing progresses, we can see the effect of epithelialization, growth of granulation tissue, some hypertrophic overgrowth, and anisotropic wound contraction.

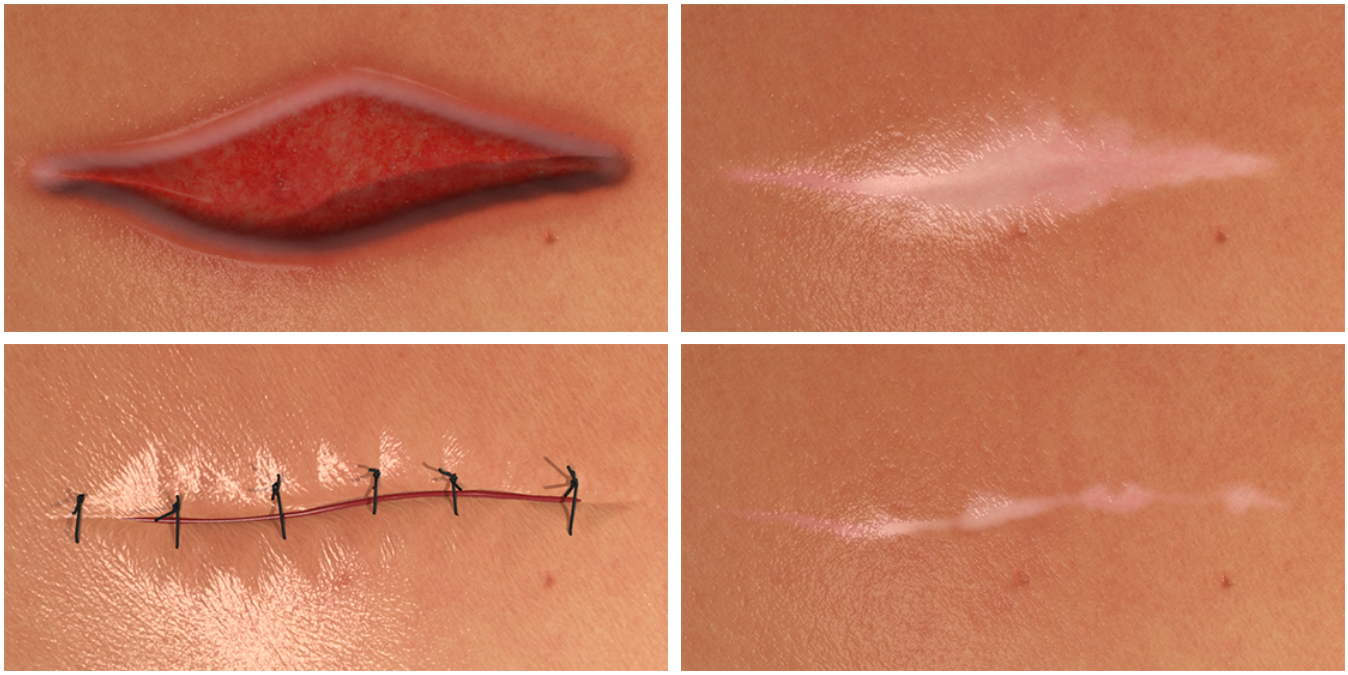

Figure 6: Wound healing with (lower pictures) and without (upper pictures) medical suturing and the resulting degree of scarring.

Figure 7: Illustration of the anisotropic contraction pulling the wound edges together and deforming the healthy surrounding skin. The main fiber direction runs horizontally here leading to a more elongated wound shape (middle) compared to the initial geometry (left). The change in the different directions in the first hours of the healing process is colored (right) using the sequence "blue (no movement), cyan, green, yellow, red (velocity of $7.715 \cdot 10^{-3}$ mm/s)".

the wound starts to mature, we can observe how the scar color gets through (the white area) and also notice a slight elevation of the scar due to the overproduction of fibrotic tissue leaving a hypertrophic scar. The grid for this simulation has a resolution of $(97, 65, 100)$ and the mass-spring simulation counts 3 734 nodes. Per frame we run sixty sub-steps of the mass-spring simulation to get a stable approximation. For the whole simulation scenario, an average simulation time of around 300 ms per frame can be measured on an Intel(R) Xeon E5 3.5 GHz with 32 GB DDR-RAM (even without GPU parallelization) which clearly demonstrate the high efficiency of the presented approach. Since it can easily be parallelized on the GPU in order to exploit the power of modern graphics hardware, huge additional speedups can be expected.

Another complex wound healing process is considered in a fifth example, in which we have simulated the healing process of a large wound on a woman's neck; see Fig. 3.

Finally, in a sixth example, the impact of suturing on the degree of scarring is studied; see Fig. 6.

7. Conclusion

We have devised a method for the efficient dynamic simulation of wound healing based on accurate models describing the underlying biochemical and biomechanical processes. Next to the reproduction of regenerative healing processes, we were able to capture specific effects like anisotropic wound contraction, scarring and scab formation in order to simulate and visualize the different stages of wound healing and their visual effects appropriately. The robustness of our approach regarding complex non-smooth input geometries has additionally been verified by simulating a healing process on a scarred face. Moreover, a complex wound healing process on a woman's neck and a medical scenario with and without suturing have been simulated accurately. The presented model is very efficient and easy to use since it can be used with realistic input parameters like those measured in biochemistry and biophysics avoiding exhausting parameter tuning or time-consuming post-processing operations. This makes the presented approach useful in the context of the modeling of humans or animals in visual computing as well as for accurate medical simulations. In addition, some artistic freedom is given in the visualization process. Moreover, the presented method is not restricted to a static input geometry, so that it can be used to study for example the negative effect of mechanical stress on the wound healing process.

8. Future Work

To reduce computational costs, blood plasma is modeled using a basic approach. Here one could think of incorporating a fluid solver with variable viscosity to accurately represent the clotting process and add more dynamics. Also we assume a non-infected wound, for which reason a possible extension would be to add debris, infection, or necrotic tissue that influences the wound shape.

For a medical use of the presented framework, a detailed clinical study is required which validates the results of the simulations against the temporal evolution of the wound healing processes of subjects. For that, accurate measurements of the specific parameters are required as well as the exact shapes of the subjects' wounds at different states of the healing processes, which have to be captured precisely including deeper layers of the skin in order to ensure similar conditions.

Acknowledgements

This work has been partially supported by the Max Planck Center for Visual Computing and Communication (MPC-VCC) funded by the Federal Ministry of Education and Research of the Federal Republic of Germany (grants FKZ-01IMC01 and FKZ-01IM10001), and the German Academic Exchange Service (DAAD) funded by the government of the Federal Republic of Germany and the European Union. The reviewers' valuable comments that improved the manuscript are gratefully acknowledged.

References

[CMU10] CUMMING B. D., MCELWAIN D. L. S., UPTON Z.: A mathematical model of wound healing and subsequent scarring. *Journal of The Royal Society Interface 7*, 42 (2010), 19–34. 2, 4

[GOH06] GASSER T. C., OGDEN R. W., HOLZAPFEL G. A.: Hyperelastic modelling of arterial layers with distributed collagen fibre orientations. *Journal of The Royal Society Interface 3*, 6 (2006), 15–35. 2, 4

[GRC*10] GURFINKEL R., ROSENBERG L., COHEN S., COHEN A., BAREZOVSKY A., CAGNANO E., SINGER A. J.: Histological assessment of tangentially excised burn eschars. *Canadian Journal of Plastic Surgery 18*, 3 (2010), e33–e36. 3

[GRM71] GABBIANI G., RYAN G. B., MAJNO G.: Presence of modified fibroblasts in granulation tissue and their possible role in wound contraction. *Experientia 27*, 5 (1971), 549–550. 3, 4

[HO10] HOLZAPFEL G. A., OGDEN R. W.: Constitutive modelling of arteries. *Proceedings of the Royal Society of London A: Mathematical, Physical and Engineering Sciences* (2010). 4

[JMDGA09] JAVIERRE E., MOREO P., DOBLARÃL' M., GARCÍA-AZNAR J.: Numerical modeling of a mechano-chemical theory for wound contraction analysis. *International Journal of Solids and Structures 46*, 20 (2009), 3597–3606. 2, 3

[KHS*83] KNIGHTON D., HUNT T., SCHEUENSTUHL H., HALLIDAY B., WERB Z., BANDA M.: Oxygen tension regulates the expression of angiogenesis factor by macrophages. *Science 221*, 4617 (1983), 1283–1285. 3

[KWP*01] KUBO M., WATER L. V. D., PLANTEFABER L. C., MOSESSON M. W., SIMON M., TONNESEN M. G., TAICHMAN L., CLARK R. A.: Fibrinogen and fibrin are anti-adhesive for keratinocytes: A mechanism for fibrin eschar slough during wound repair. *Journal of Investigative Dermatology 117*, 6 (2001), 1369–1381. 3

[LLC11] LEE C.-Y., LEE S., CHIN S.: Multi-layer structural wound synthesis on 3D face. *Computer Animation and Virtual Worlds 22*, 2-3 (Apr. 2011), 177–185. 2

[LSNP13] LI D., SUEDA S., NEOG D. R., PAI D. K.: Thin skin elastodynamics. In *ACM Transactions on Graphics* (New York, NY, USA, 2013), SIGGRAPH '13, ACM, pp. 49:1–49:9. 1

[LST09] LEE S.-H., SIFAKIS E., TERZOPOULOS D.: Comprehensive biomechanical modeling and simulation of the upper body. *ACM Transactions on Graphics 28*, 4 (2009), 99:1–99:17. 2

[MGAD08] MOREO P., GARCÍA-AZNAR J. M., DOBLARÉ M.: Modeling mechanosensing and its effect on the migration and proliferation of adherent cells. *Acta Biomaterialia 4*, 3 (2008), 613–621. 4

[MZS*11] MCADAMS A., ZHU Y., SELLE A., EMPEY M., TAMSTORF R., TERAN J., SIFAKIS E.: Efficient elasticity for character skinning with contact and collisions. *ACM Transactions on Graphics 30*, 4 (July 2011), 37:1–37:12. 1

[Nag15] NAGANO K.: Skin stretch: Simulating dynamic skin microgeometry. In *ACM SIGGRAPH 2015 Computer Animation Festival* (New York, NY, USA, 2015), ACM, pp. 133–133. 1

[OB09] ORGILL D., BLANCO C.: 15 – Summary: biomaterials for treating skin loss. In *Biomaterials for Treating Skin Loss*, Orgill D., Blanco C., (Eds.), Woodhead Publishing Series in Biomaterials. Woodhead Publishing, 2009, pp. 231–235. 2

[OSM95] OLSEN L., SHERRATT J. A., MAINI P. K.: A mechanochemical model for adult dermal wound contraction and the permanence of the contracted tissue displacement profile. *Journal of Theoretical Biology 177*, 2 (1995), 113–128. 2

[Si15] SI H.: Tetgen, a delaunay-based quality tetrahedral mesh generator. *ACM Transactions on Mathematical Software 41*, 2 (2015), 11:1–11:36. 5

[Sif07] SIFAKIS E.: *Algorithmic Aspects of the Simulation and Control of Computer Generated Human Anatomy Models*. PhD thesis, Stanford University, 2007. 2

[SKB08] STEFFEN M., KIRBY R. M., BERZINS M.: Analysis and reduction of quadrature errors in the material point method (mpm). *International Journal for Numerical Methods in Engineering 76*, 6 (2008), 922–948. 5

[SM91] SHERRATT J. A., MURRAY J. D.: Mathematical analysis of a basic model for epidermal wound healing. *Journal of Mathematical Biology 29*, 5 (1991), 389–404. 2

[TBHF03] TERAN J., BLEMKER S., HING V. N. T., FEDKIW R.: Finite volume methods for the simulation of skeletal muscle. In *Proceedings of the 2003 ACM SIGGRAPH/Eurographics Symposium on Computer Animation* (Aire-la-Ville, Switzerland, Switzerland, 2003), SCA '03, Eurographics Association, pp. 68–74. 1

[UF11] UEDA K., FUJISHIRO I.: Visual simulation of bleeding on skin surface. In *ACM Transactions on Graphics* (New York, NY, USA, 2011), SIGGRAPH '11, ACM, pp. 9:1–9:1. 2

[VBG*13] VAILLANT R., BARTHE L., GUENNEBAUD G., CANI M.-P., ROHMER D., WYVILL B., GOURMEL O., PAULIN M.: Implicit skinning: Real-time skin deformation with contact modeling. In *ACM Transactions on Graphics* (New York, NY, USA, 2013), SIGGRAPH '13, ACM, pp. 125:1–125:12. 2

[VJGAGB12] VALERO C., JAVIERRE E., GARCÍA-AZNAR J. M., GÓMEZ-BENITO M. J.: Numerical modelling of the angiogenesis process in wound contraction. *Biomechanics and Modeling in Mechanobiology 12*, 2 (2012), 349–360. 3, 4, 6

[VJGAGB14] VALERO C., JAVIERRE E., GARCÍA-AZNAR J. M., GOMEZ-BENITO M. J.: A cell-regulatory mechanism involving feedback between contraction and tissue formation guides wound healing progression. *PLOS ONE 9* (2014). 2, 3, 4